Nuclear Engineering and Technology 52 (2020) 485–498

Contents lists available at ScienceDirect

Nuclear Engineering and Technology

journal homepage: www.elsevier.com/locate/net

Original Article

Diffusion synthetic acceleration with the fine mesh rebalance of the subcell balance method with tetrahedral meshes for S_N transport calculations

Habib Muhammad, Ser Gi Hong*

Department of Nuclear Engineering, Kyung Hee University, Deogyeong-daero, GiHeung-gu, Yongin, Gyeonggi-do, 446-701, South Korea

ARTICLE INFO

Article history:
Received 16 July 2019
Received in revised form
23 August 2019
Accepted 27 August 2019
Available online 28 August 2019

Keywords:
Neutron transport equation
Diffusion equation
DFEM
LDEM-SCB
Tetrahedral mesh

ABSTRACT

A diffusion synthetic acceleration (DSA) technique for the S_N transport equation discretized with the linear discontinuous expansion method with subcell balance (LDEM-SCB) on unstructured tetrahedral meshes is presented. The LDEM-SCB scheme solves the transport equation with the discrete ordinates method by using the subcell balances and linear discontinuous expansion of the flux. Discretized DSA equations are derived by consistently discretizing the continuous diffusion equation with the LDEM-SCB method, however, the discretized diffusion equations are not fully consistent with the discretized transport equations. In addition, a fine mesh rebalance (FMR) method is devised to accelerate the discretized diffusion equation coupled with the preconditioned conjugate gradient (CG) method. The DSA method is applied to various test problems to show its effectiveness in speeding up the iterative convergence of the transport equation. The results show that the DSA method gives small spectral radii for the tetrahedral meshes having various minimum aspect ratios even in highly scattering dominant mediums for the homogeneous test problems. The numerical tests for the homogeneous and heterogeneous problems show that DSA with FMR (with preconditioned CG) gives significantly higher speedups and robustness than the one with the Gauss-Seidel-like iteration.

1. Introduction

For the past few decades, there have been considerable efforts to devise accurate spatial discretization methods for the multi-group transport equation on unstructured meshes such as tetrahedral meshes. The discontinuous finite element method (DFEM) is one of the famous methods of solving the transport equation with unstructured meshes [1–6]. Hong developed a new method called LDEM-SCB, which uses subcell balances for tetrahedral meshes and linear discontinuous expansion of the flux [4]. Allowing flux discontinuities on the interface provides better robustness and accuracy than the continuous finite element methods (FEMs). In particular, LDEM-SCB was developed to increase the robustness (particularly positivity) of the flux without the loss of accuracy in comparison with DFEM, as shown in the previous work [4]. In this method, the subcell balances over four subcells for each tetrahedral mesh are used to obtain the coupling equations, which give the relationships among the unknown fluxes. On the other hand, no acceleration method has been applied to LDEM-SCB.

However, the iterative solutions of the transport equations with the source iteration converge very slowly in highly scattering dominant problems of optically thick size. Therefore, research on developing fast and efficient methods to accelerate the convergence of the source iteration has been a strong focus in the nuclear engineering community [7]. One such method, the diffusion synthetic acceleration, is a very powerful method to accelerate the convergence of the source iteration of the neutron transport equation [8–14]. However, the development of an efficient DSA for the discretized transport method using unstructured geometry such as tetrahedral mesh for the complicated geometrical problems is not straightforward because a certain level of consistency between the discretized diffusion and transport equations is required to achieve the unconditional stability of the convergence [1–3,7–15]. As a result, several methods have been suggested for accelerating the iterative solution of DFEM for the transport equation. First, Adams and Martin derived a modified four-step (M4S) DSA scheme for the discrete ordinates transport equations

* Corresponding author.
E-mail addresses: mhspecialisttt@gmail.com (H. Muhammad), sergihong@khu.ac.kr (S.G. Hong).

https://doi.org/10.1016/j.net.2019.08.021

discretized with DFEM [9]. Similar to Khalil's approach [10], they derived the discretized diffusion equation by consistently discretizing the continuous diffusion equation to DFEM by coupling the current mesh with its adjacent meshes through the incoming partial currents. This method is not fully consistent with DFEM of the discrete ordinates transport equation, but they showed that this method gives unconditionally stable and rapid convergence for one-dimensional slab and two-dimensional Cartesian geometries. However, this method was unstable on three-dimensional unstructured tetrahedral meshes for the problems with low aspect ratios [11].

On the other hand, the fully consistent DSA (FCDSA) was derived on unstructured tetrahedral meshes. This method maintains the unconditional stability and effectiveness for various minimum aspect ratios of meshes in the homogeneous problems [11]. However, this method has drawbacks in that the consistently derived diffusion equation is very costly to solve, even with a preconditioner, and it loses its effectiveness in multidimensional problems with material discontinuities [13]. Warsa et al. also studied the application of the Krylov methods with DSA as a preconditioner [16]. For the problems with material discontinuities, they showed that this approach (particularly with a partially consistent DSA as a preconditioner) can be effectively used for the problems that are intractable by the source iteration and DSA.

In this work, a diffusion synthetic acceleration method is devised by consistently discretizing the continuous diffusion equation to LDEM-SCB(1) with the procedure suggested by Adams and Martin [9]. However, the discretized DSA equations are not fully consistent with the discretized LDEM-SCB(1) equations. As in LDEM-SCB(1), the scalar flux correction is approximated using the linear discontinuous expansion in each tetrahedral mesh, which leads to four unknowns (*i.e.,* four scalar flux corrections at the four nodes). Then, the coupling equations for the four unknown scalar flux corrections are derived by using the subcell balance equations over the four subcells that are considered in LDEM-SCB(1). The net current correction terms appearing in the subcell balance equations are decomposed into the incoming and outgoing partial current corrections. Outgoing partial current corrections are represented in terms of unknowns in the current mesh, while the incoming ones are represented in terms of unknowns in the upstream meshes from which the neutrons flow. The resulting DSA equations form a linear discontinuous discretization of the continuous diffusion equation. They were first iteratively solved using the Gauss-Seidel (GS)-like method, but this iterative scheme was shown to be ineffective for large problems having a high scattering ratio.

In this work, we newly suggest a fine mesh rebalance (FMR) method coupled with the conjugate gradient (CG) method to accelerate the GS-like iteration of the discretized diffusion equation. To show the effectiveness of the DSA method coupled with FMR, we applied them to several homogeneous and heterogeneous test problems. To improve the overall efficiency of DSA(FMR) applied to LDEM-SCB(1), we applied the Jacobi and the split preconditioners to CG [17]. We also showed the effect of the shape of the tetrahedral mesh with various aspect ratios for a homogeneous problem. The numerical estimates of the spectral radius, the number of iterations, and the computing times were used to measure the effectiveness because the DSA Fourier analysis has yet not been performed.

In Sec. 2.1, the LDEM-SCB(1) method is reviewed. The methodologies for DSA for LDEM-SCB(1) and FMR are given in Sec. 2.2 and Sec. 2.3, respectively. The numerical tests to show the effectiveness of the suggested DSA method with FMR are given in Sec. 3. Finally, the summary and conclusion are given in Sec. 4.

2. Theory and formulation

2.1. Review of LDEM-SCB(1)

The within-group discrete ordinates transport equation with isotropic scattering is given by

$$\widehat{\Omega}_m \cdot \nabla \psi_m^{(\ell+1/2)}(\vec{r}) + \sigma_t \psi_m^{(\ell+1/2)}(\vec{r}) = \sigma_s \phi^{(\ell)}(\vec{r}) + q, \tag{1}$$

where ψ_m is the angular flux in the direction $\widehat{\Omega}_m$, ϕ is the scalar flux, σ_t is the macroscopic total cross-section, σ_s is the macroscopic scattering cross-section and q is the within-group source, which includes the scattering sources from other groups, fission source, and the external sources. In Eq. (1), ℓ represents the source iteration index. Hong developed a subcell balance method LDEM-SCB for solving the S_N transport equation on unstructured tetrahedral meshes by splitting the tetrahedral mesh into four subcells [4]. The LDEM-SCB method uses the linear expansion of fluxes in each mesh and the subcell balance equations over four subcells to obtain the coupling equations for unknown fluxes rather than the Galerkin method for each direction. In this method, the meshes are coupled through the incoming interface fluxes from the upstream meshes as in DFEM. Therefore, the conventional sweeping procedure can be used in LDEM-SCB on tetrahedral meshes for complicated geometrical problems [1,4].

Two subcell balance methods were developed for solving the multigroup S_N transport equation by dividing each tetrahedral mesh into four subcells in two ways. Fig. 1 shows the cell division for LDEM-SCB(1) in which each subcell is formed by using the tetrahedron's center point, three face-centered points, three edge-centered points, and one node point [4]. Each subcell is a hexahedron that is related to three external faces and three internal faces. Each external face is divided into three subfaces. Each subcell is denoted with the node number it contains. That is to say, the subcell containing a node α is denoted by the subcell α.

The angular flux and source are expanded in each tetrahedron by using the following linear expansion:

$$\psi^k(x,y,z) = \varphi_1^k + x\varphi_2^k + y\varphi_3^k + z\varphi_4^k, \tag{2}$$

where φ_i^k represents the *i'th* expansion coefficient of the angular flux for the tetrahedral mesh k. In Eq. (2), x, y, and z represent the global Cartesian coordinates. In this paper, we omitted the direction

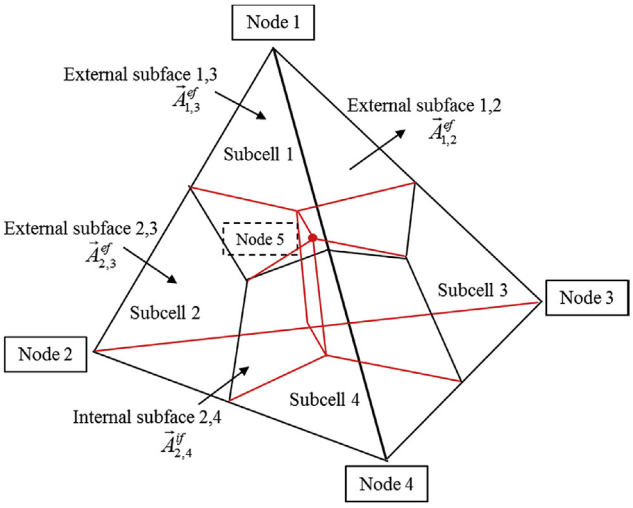

Fig. 1. Subcell division for LDEM-SCB(1).

index (m) for simplicity. The simple algebra shows that the average flux over the external subface $A^{ef}_{\alpha,\beta}$ characterized by a node α and an external face β (see Fig. 1) can be expressed in terms of expansion coefficients as follows:

$$\psi^{k,ef}_{\alpha,\beta} = \varphi^k_1 + \frac{1}{36}(22x_\alpha + 7x_\gamma + 7x_\delta)\varphi^k_2 + \frac{1}{36}(22y_\alpha + 7y_\gamma + 7y_\delta)\varphi^k_3 + \frac{1}{36}(22z_\alpha + 7z_\gamma + 7z_\delta)\varphi^k_4, \tag{3}$$

where x_α, y_α, and z_α represent the x, y, and z coordinates of node α, respectively. In Eq. (3), γ and δ are the other nodes' indices (different from node α) of the external face β.

On the other hand, the average flux over the internal face $A^{if}_{\alpha,\beta}$, which represents the interface between subcell α and subcell β, is given by

$$\psi^{k,if}_{\alpha,\beta} = \varphi^k_1 + \frac{1}{36}(6x_\alpha + 6x_\beta - 2x_\gamma - 2x_\delta)\varphi^k_2 + \frac{1}{36}(6y_\alpha + 6y_\beta - 2y_\gamma - 2y_\delta)\varphi^k_3 + \frac{1}{36}(6z_\alpha + 6z_\beta - 2z_\gamma - 2z_\delta)\varphi^k_4. \tag{4}$$

Similarly, the subcell average flux is represented by

$$\psi^k_{sc,\alpha} = \varphi^k_1 + \frac{13}{36}x_\alpha\varphi^k_2 + \frac{13}{36}y_\alpha\varphi^k_3 + \frac{13}{36}z_\alpha\varphi^k_4. \tag{5}$$

Then, the representations of the internal face average flux and external subface average flux in terms of the subcell average fluxes are given by

$$\psi^{k,if}_{\alpha,\beta} = \frac{29}{52}\left(\psi^k_{sc,\alpha} + \psi^k_{sc,\beta}\right) - \frac{3}{52}\left(\psi^k_{sc,\gamma} + \psi^k_{sc,\delta}\right), \tag{6}$$

$$\psi^{k,ef}_{\alpha,\beta} = \frac{1}{52}\left(65\psi^k_{sc,\alpha} - 23\psi^k_{sc,\beta} + 5\psi^k_{sc,\gamma} + 5\psi^k_{sc,\delta}\right). \tag{7}$$

It can be shown that the subcell average flux is represented in terms of the point fluxes at the nodes as follows:

$$\psi^k_{sc,\alpha} = \frac{75}{144}\psi^k_\alpha + \frac{23}{144}\left(\psi^k_\beta + \psi^k_\gamma + \psi^k_\delta\right), \tag{8}$$

where ψ^k_α represents the flux at node α of mesh k.

The LDEM-SCB(1) method uses the subcell balance equations to couple the unknown point angular fluxes. For example, the balance equation over subcell 1 is given by

$$\frac{1}{3}\hat{\Omega}\cdot\vec{A}_2\psi^{k,ef}_{1,2} + \frac{1}{3}\hat{\Omega}\cdot\vec{A}_3\psi^{k,ef}_{1,3} + \frac{1}{3}\hat{\Omega}\cdot\vec{A}_4\psi^{k,ef}_{1,4} + \hat{\Omega}\cdot\vec{A}^{if}_{1,2}\psi^{k,if}_{1,2} + \hat{\Omega}\cdot\vec{A}^{if}_{1,3}\psi^{k,if}_{1,3} + \hat{\Omega}\cdot\vec{A}^{if}_{1,4}\psi^{k,if}_{1,4} + \sigma^k V^k_{sc1}\psi^k_{sc1} = q^k_{sc1}V^k_{sc1}. \tag{9}$$

In Eq. (9), the source is given by

$$q^k_{sc1} = \sigma^k_s\phi^k_{sc1} + s^k_{sc1}. \tag{10}$$

In Eq. (10), s^k_{sc1} represents the within-group source. The internal face vectors between subcell 1 and subcells 2, 3 and 4, respectively, are given by

$$\vec{A}^{if}_{1,2} = \frac{1}{12}\vec{A}_1 - \frac{1}{12}\vec{A}_2,\quad \vec{A}^{if}_{1,3} = \frac{1}{12}\vec{A}_1 - \frac{1}{12}\vec{A}_3,\quad \vec{A}^{if}_{1,4} = \frac{1}{12}\vec{A}_1 - \frac{1}{12}\vec{A}_4. \tag{11}$$

The substitution of Eqs. (6), (7) and (11) into Eq. (9) (after representing them in terms of point fluxes using Eq. (8)) gives the final subcell balance equation for subcell 1 in terms of point fluxes:

$$\begin{aligned}
&\left\{\frac{13}{108}\vec{A}_1\cdot\hat{\Omega} + \frac{22}{108}\left(\delta^0_2\vec{A}_2 + \delta^0_3\vec{A}_3 + \delta^0_4\vec{A}_4\right)\cdot\hat{\Omega} + \frac{75}{144}\sigma^k V^k_{sc1}\right\}\psi^k_1 \\
&+\left\{\frac{7}{108}\vec{A}_1\cdot\hat{\Omega} - \frac{2}{108}\vec{A}_2\cdot\hat{\Omega} + \frac{7}{108}\delta^0_3\vec{A}_3\cdot\hat{\Omega} + \frac{7}{108}\delta^0_4\vec{A}_4\cdot\hat{\Omega} + \frac{23}{144}\sigma^k V^k_{sc1}\right\}\psi^k_2 \\
&+\left\{\frac{7}{108}\vec{A}_1\cdot\hat{\Omega} + \frac{7}{108}\delta^0_2\vec{A}_2\cdot\hat{\Omega} - \frac{2}{108}\vec{A}_3\cdot\hat{\Omega} + \frac{7}{108}\delta^0_4\vec{A}_4\cdot\hat{\Omega} + \frac{23}{144}\sigma^k V^k_{sc1}\right\}\psi^k_3 \\
&+\left\{\frac{7}{108}\vec{A}_1\cdot\hat{\Omega} + \frac{7}{108}\delta^0_2\vec{A}_2\cdot\hat{\Omega} + \frac{7}{108}\delta^0_3\vec{A}_3\cdot\hat{\Omega} - \frac{2}{108}\vec{A}_4\cdot\hat{\Omega} + \frac{23}{144}\sigma^k V^k_{sc1}\right\}\psi^k_4 \\
&= \left\{\frac{75}{144}q^k_{sc1} + \frac{23}{144}\left(q^k_{sc2} + q^k_{sc3} + q^k_{sc4}\right)\right\}V^k_{sc1} - \frac{1}{108}\delta^0_2\vec{A}_2\cdot\hat{\Omega}\left(22\psi^{k'_2,ups}_1 + 7\psi^{k'_2,ups}_3 + 7\psi^{k'_2,ups}_4\right) \\
&-\frac{1}{108}\delta^0_3\vec{A}_3\cdot\hat{\Omega}\left(22\psi^{k'_3,ups}_1 + 7\psi^{k'_3,ups}_2 + 7\psi^{k'_3,ups}_4\right) - \frac{1}{108}\delta^0_4\vec{A}_4\cdot\hat{\Omega}\left(22\psi^{k'_4,ups}_1 + 7\psi^{k'_4,ups}_2 + 7\psi^{k'_4,ups}_3\right),
\end{aligned} \tag{12}$$

where k'_α represents the mesh adjacent to the external face A_α of the current mesh k, and the function δ^0_α is defined by

$$\delta^0_\alpha = \begin{pmatrix} 1, & if\ \hat{\Omega}\cdot\vec{A}_\alpha\rangle 0, \\ 0, & if\ \hat{\Omega}\cdot\vec{A}_\alpha\langle 0, \end{pmatrix}. \tag{13}$$

Eq. (12) represents the balance equation for subcell 1 and three similar equations can be derived for the other three subcells with the same procedure.

The set of these four transport subcell equations are solved using a GS-like iteration method for each direction with a sweeping procedure and the source iteration. In a highly scattering dominant problem of optically thick size, the GS-like iteration method with the source iteration becomes slow. Therefore, an acceleration method is always needed to accelerate the convergence of the source iteration.

2.2. Derivation of DSA equations

In this section, the DSA equations are derived by consistently

discretizing the continuous diffusion equations using the LDEM-SCB(1) method. This approach is similar to that suggested by Adams and Martin [9]. That is to say, the continuous diffusion equation is discretized with the same manner used in the LDEM-SCB(1) discretization. The derivation of the DSA equations starts with the following continuous diffusion equation:

$$\nabla \cdot \vec{F}^{(\ell+1)}(\vec{r}) + \sigma_a f^{(\ell+1)}(\vec{r}) = q^{(\ell+1/2)}(\vec{r}), \tag{14}$$

$$\frac{1}{3}\nabla f^{(\ell+1)}(\vec{r}) + \sigma_t \vec{F}^{(\ell+1)}(\vec{r}) = 0, \tag{15}$$

where the source q, the scalar flux correction f, and the net current correction vector $\vec{F}$ are given by

$$\begin{aligned} q^{(\ell+1/2)}(\vec{r}) &= \sigma_s\left(\phi^{(\ell+1/2)}(\vec{r}) - \phi^{(\ell)}(\vec{r})\right), \\ \phi^{(\ell+1)}(\vec{r}) &= \phi^{(\ell+1/2)}(\vec{r}) + f^{(\ell+1)}(\vec{r}), \\ \vec{J}^{(\ell+1)}(\vec{r}) &= \vec{J}^{(\ell+1/2)}(\vec{r}) + \vec{F}^{(\ell+1)}(\vec{r}), \end{aligned} \tag{16}$$

where ϕ and $\vec{J}$ represent the scalar flux and net current, respectively. The scalar flux is defined as follows:

$$\phi^{(\ell+1/2)} = \int_{4\pi} d\hat{\Omega}\psi^{(\ell+1/2)}. \tag{17}$$

In Eq. (16), the quantities having iteration index $(\ell+1/2)$ represent the results of a transport sweep using LDEM-SCB(1), while the ones having indices $(\ell+1)$ and (ℓ) represent the results obtained with DSA and the flux before the transport sweeping, respectively.

The continuous diffusion equations (*i.e.,* Eqs. (14) and (15)) are discretized in a manner consistent with LDEM-SCB(1), but this derivation of DSA is not fully consistent with the discretized transport equation. First, the subcell balance equations are obtained by integrating Eq. (14) over a subcell. For example, the balance equation over the first subcell of a tetrahedron mesh k is given by

$$\int_{V^k_{sc1}} \nabla \cdot \vec{F}^{k,(\ell+1)} dV + \int_{V^k_{sc1}} \sigma^k_a f^{k,(\ell+1)} dV = \int_{V^k_{sc1}} q^{k,(\ell+1/2)} dV, \tag{18}$$

where σ^k_a is the macroscopic absorption cross-section and V^k_{sc1} is the volume of subcell 1. Applying the divergence theorem to Eq. (18) after dropping the iteration indices gives

$$\int_{A_{sc1}} dA\left(\vec{F}^k \cdot \hat{n}\right) + \sigma^k_a \bar{f}^k_{sc1} V^k_{sc1} = \bar{q}^k_{sc1} V^k_{sc1}, \tag{19}$$

where $\bar{f}^k_{sc1}$ and $\bar{q}^k_{sc1}$ are the average values of the scalar flux correction and the source, respectively, over subcell 1 of mesh k. This subcell balance equation can be rewritten by decomposing the surface integral into external and interface surface terms as follows:

$$\left(\vec{F}^{k,ef}_{1,2}\cdot\vec{A}^{k,ef}_{1,2} + \vec{F}^{k,ef}_{1,3}\cdot\vec{A}^{k,ef}_{1,3} + \vec{F}^{k,ef}_{1,4}\cdot\vec{A}^{k,ef}_{1,4}\right) + \left(\vec{F}^{k,if}_{1,2}\cdot\vec{A}^{k,if}_{1,2} + \vec{F}^{k,if}_{1,3}\cdot\vec{A}^{k,if}_{1,3} + \vec{F}^{k,if}_{1,4}\cdot\vec{A}^{k,if}_{1,4}\right) + \sigma^k_a \bar{f}^k_{sc1} V^k_{sc1} = \bar{q}^k_{sc1} V^k_{sc1}, \tag{20}$$

where the superscripts *ef* and *if* refer to the external and internal subfaces, respectively, and the subscripts in the net current corrections $\vec{F}$ and area vector $\vec{A}$ refer to the node and face numbers associated with subcell 1 of mesh k. For example, $\vec{F}^{k,ef}_{1,2}$ represents the average current correction over the external subface $\vec{A}^{k,ef}_{1,2}$ of subcell 1, whereas $\vec{A}^{k,ef}_{1,2}$ represents the external subface, which is opposite to node-2 of subcell 1 as shown in Fig. 1. For the external subface $\vec{A}^{k,ef}_{1,2}$, the net current correction is expressed in terms of partial current corrections as follows:

$$\vec{F}^{k,ef}_{1,2} \cdot \vec{A}^{k,ef}_{1,2} = \left|\vec{A}^{k,ef}_{1,2}\right|\left(\vec{F}^{k,ef}_{1,2} \cdot \hat{n}^k_2\right), \tag{21}$$

where $\hat{n}^k_2$ is the outer normal vector of $\vec{A}^{k,ef}_{1,2}$, and $\vec{A}^k_2$ is the external surface area vector opposite to node-2 (*i.e.,* $\vec{A}^{k,ef}_{1,2} = \vec{A}^k_2/3$).

$$\left|\vec{A}^{k,ef}_{1,2}\right|\left(\vec{F}^{k,ef}_{1,2} \cdot \hat{n}^k_2\right) = \frac{1}{3}\left|\vec{A}^k_2\right|\left(w_2 F^{k,ef,+}_{1,2} - v_2 F^{k'(1,2),ef,+}_{\alpha',\beta'}\right), \tag{22}$$

where $F^{k,ef,+}_{1,2}$ and $F^{k'(1,2),ef,+}_{\alpha',\beta'}$ represent the outgoing and incoming partial current corrections respectively, across the external subface $\vec{A}^{k,ef}_{1,2}$ from the viewpoint of mesh k. The index $k'(1,2)$ in Eq. (22) represents the neighboring mesh of the present mesh k through the subface $\vec{A}^{k,ef}_{1,2}$, while α' and β' are the local node indices of mesh $k'(1,2)$, and they specify the subface $\vec{A}^{k,ef}_{1,2}$.

In Eq. (22), the parameters w_2 and v_2 represent the outgoing and incoming boundary conditions, respectively, on the face $\vec{A}^k_2$ of mesh k on the external boundary. The external boundary conditions are generalized as

$$\begin{matrix}\text{Vacuum B.C.}\\ \text{Reflective B.C.}\\ \text{Interface}\end{matrix} = \begin{cases} w = 1, v = 0, \\ w = 0, v = 0, \\ w = 1, v = 1. \end{cases} \tag{23}$$

The outgoing partial current correction from mesh k through the external subface with the P_1 approximation is given by

$$F^{k,ef,+}_{1,2} = \frac{1}{4}f^k_{1,2} - \frac{1}{2}D^k\left(\hat{n}^k_2 \cdot \nabla f^k\right), \tag{24}$$

where D^k is the diffusion coefficient, $f^k_{1,2}$ is the average scalar flux correction over the external subface $\vec{A}^{k,ef}_{1,2}$, whereas A^k_{2x}, A^k_{2y}, and A^k_{2z} represent x, y, and z-components of the vector $\vec{A}^k_2$.

$$f^k_{1,2} = \frac{22}{36}f^k_1 + \frac{7}{36}\left(f^k_3 + f^k_4\right). \tag{25}$$

The dot product of $\hat{n}^k_2$ and ∇f^k is given by

$$\hat{n}_2^k \cdot \nabla f^k = \left(A_{2x}^k \frac{\partial f^k}{\partial x} + A_{2y}^k \frac{\partial f^k}{\partial y} + A_{2z}^k \frac{\partial f^k}{\partial z} \right). \tag{26}$$

The substitution of Eqs. (25) and (26) into Eq. (24) gives the outgoing partial current correction.

$$F_{1,2}^{k,ef,+} = \frac{1}{144}\left(22f_1^k + 7f_3^k + 7f_4^k\right) - \frac{D^k}{2\left|\overrightarrow{A}_2^k\right|}\left(A_{2x}^k \frac{\partial f^k}{\partial x} + A_{2y}^k \frac{\partial f^k}{\partial y} + A_{2z}^k \frac{\partial f^k}{\partial z} \right). \tag{27}$$

Similarly, the incoming partial current correction from mesh $k'(1,2)$ (note that it is the outgoing partial current correction from the viewpoint of this neighboring mesh) is given by

$$F_{\alpha',\beta'}^{k'(1,2),ef,+} = \frac{1}{4} f_{\alpha',\beta'}^{k'(1,2)} + \frac{1}{2} D^{k'(1,2)} \left(\hat{n}_{\beta'}^{k'(1,2)} \cdot \nabla f^{k'(1,2)} \right), \tag{28}$$

where the outward normal unit vector is $\hat{n}_{\beta'}^{k'(1,2)} = -\hat{n}_2^k$. The scalar flux correction $f_{\alpha',\beta'}^{k'(1,2)}$ over external subface $\overrightarrow{A}_{\alpha',\beta'}^{k'(1,2),ef}$ of mesh $k'(1,2)$ adjacent to mesh k through the subface (*i.e.*, $\overrightarrow{A}_{1,2}^{k,ef} = -\overrightarrow{A}_{\alpha',\beta'}^{k'(1,2),ef}$) is given by

$$f_{\alpha',\beta'}^{k'(1,2)} = \frac{22}{36} f_{\alpha'}^{k'(1,2)} + \frac{7}{36}\left(f_{\gamma'}^{k'(1,2)} + f_{\delta'}^{k'(1,2)} \right). \tag{29}$$

In Eq. (29), $f_{\alpha'}^{k'(1,2)}$, $f_{\gamma'}^{k'(1,2)}$ and $f_{\delta'}^{k'(1,2)}$ represent the scalar flux correction at nodes α', γ' and δ' of mesh $k'(1,2)$, respectively. The incoming partial current correction is given by

$$F_{\alpha',\beta'}^{k'(1,2),ef,+} = \frac{1}{144}\left(22f_{\alpha'}^{k'(1,2)} + 7f_{\gamma'}^{k'(1,2)} + 7f_{\delta'}^{k'(1,2)}\right) + \frac{D^{k'(1,2)}}{2\left|\overrightarrow{A}_2^k\right|}\left(A_{2x}^k \frac{\partial f^{k'(1,2)}}{\partial x'} + A_{2y}^k \frac{\partial f^{k'(1,2)}}{\partial y'} + A_{2z}^k \frac{\partial f^{k'(1,2)}}{\partial z'} \right). \tag{30}$$

To further simplify Eqs. (27) and (30), we use the barycentric transformation between the global coordinates (x,y,z) and the local coordinates $(\xi_1,\xi_2,\xi_3,\xi_4)$ systems. Any linear function $g(x,y,z)$ taking its values $g_i (i=1,2,3,4)$ at the nodes of a tetrahedron can be represented in terms of the local barycentric coordinates as follows:

$$g(\xi_1,\xi_2,\xi_3,\xi_4) = g_1\xi_1 + g_2\xi_2 + g_3\xi_3 + g_4\xi_4, \tag{31}$$

where $\xi_4 = 1 - \xi_1 - \xi_2 - \xi_3$. This transformation is illustrated in Fig. 2.

The 4×4 Jacobian matrix for the tetrahedron between the global and local barycentric coordinates is given by

$$\begin{bmatrix} 1 \\ x \\ y \\ z \end{bmatrix} = \begin{bmatrix} 1 & 1 & 1 & 1 \\ x_1 & x_2 & x_3 & x_4 \\ y_1 & y_2 & y_3 & y_4 \\ z_1 & z_2 & z_3 & z_4 \end{bmatrix} \begin{bmatrix} \xi_1 \\ \xi_2 \\ \xi_3 \\ \xi_4 \end{bmatrix}. \tag{32}$$

The explicit inversion of the transformation given in Eq. (32) gives

where

$$\begin{bmatrix} \xi_1 \\ \xi_2 \\ \xi_3 \\ \xi_4 \end{bmatrix} = \frac{1}{6V^k} \begin{bmatrix} 6V_{01} & y_{42}z_{32} - z_{42}y_{32} & x_{32}z_{42} - x_{42}z_{32} & x_{42}y_{32} - x_{32}y_{42} \\ 6V_{02} & y_{31}z_{43} - z_{34}y_{13} & x_{43}z_{31} - x_{13}z_{34} & x_{31}y_{43} - x_{34}y_{13} \\ 6V_{03} & y_{24}z_{14} - z_{14}y_{24} & x_{14}z_{24} - x_{24}z_{14} & x_{24}y_{14} - x_{14}y_{24} \\ 6V_{04} & y_{13}z_{21} - z_{12}y_{31} & x_{21}z_{13} - x_{31}z_{12} & x_{13}y_{21} - x_{12}y_{31} \end{bmatrix} \begin{bmatrix} 1 \\ x \\ y \\ z \end{bmatrix}, \tag{33}$$

$$u_{\alpha\beta} = u_\beta - u_\alpha, \quad u = x,y,z.$$

In Eq. (33), the following definitions are used:

$$\begin{aligned} V^k &= V_{01} + V_{02} + V_{03} + V_{04}, \\ 6V_{01} &= x_2(y_3z_4 - y_4z_3) + x_3(y_4z_2 - y_2z_4) + x_4(y_2z_3 - y_3z_2), \\ 6V_{02} &= x_1(z_4y_3 - y_3z_4) + x_3(y_1z_4 - y_4z_1) + x_4(y_3z_1 - y_1z_3), \\ 6V_{03} &= x_1(y_2z_4 - y_4z_2) + x_2(y_4z_1 - y_1z_4) + x_4(y_1z_2 - y_2z_1), \\ 6V_{04} &= x_1(y_3z_2 - y_2z_3) + x_2(y_1z_3 - y_3z_1) + x_3(y_2z_1 - y_1z_2). \end{aligned} \tag{34}$$

The components of the external face area vectors can be expressed as

$$\begin{aligned} &y_{42}z_{32} - z_{32}y_{42} = -2A_{1x}, \quad x_{32}z_{42} - x_{42}z_{32} = -2A_{1y}, \quad x_{42}y_{32} - x_{32}y_{42} = -2A_{1z}, \\ &y_{31}z_{43} - z_{34}y_{13} = -2A_{2x}, \quad x_{43}z_{31} - x_{13}z_{34} = -2A_{2y}, \quad x_{31}y_{43} - x_{34}y_{13} = -2A_{2z}, \\ &y_{24}z_{14} - z_{14}y_{24} = -2A_{3x}, \quad x_{14}z_{24} - x_{24}z_{14} = -2A_{3y}, \quad x_{24}y_{14} - x_{14}y_{24} = -2A_{3z}, \\ &y_{13}z_{21} - z_{12}y_{31} = -2A_{4x}, \quad x_{21}z_{13} - x_{31}z_{12} = -2A_{4y}, \quad x_{13}y_{21} - x_{12}y_{31} = -2A_{4z}. \end{aligned} \tag{35}$$

The substitution of Eq. (35) into Eq. (33) gives

$$\begin{bmatrix} \xi_1 \\ \xi_2 \\ \xi_3 \\ \xi_4 \end{bmatrix} = -\frac{1}{3V^k} \begin{bmatrix} 6V_{01} & A_{1x} & A_{1y} & A_{1z} \\ 6V_{02} & A_{2x} & A_{2y} & A_{2z} \\ 6V_{03} & A_{3x} & A_{3y} & A_{3z} \\ 6V_{04} & A_{4x} & A_{4y} & A_{4z} \end{bmatrix} \begin{bmatrix} 1 \\ x \\ y \\ z \end{bmatrix}. \tag{36}$$

Next, the scalar flux correction is expanded in terms of local coordinates as follows:

$$f^k = \xi_1 f_1^k + \xi_2 f_2^k + \xi_3 f_3^k + \xi_4 f_4^k. \tag{37}$$

Then, the partial derivatives of scalar flux correction with respect to x, y, and z are given by

$$\frac{\partial f^k}{\partial x}=f_1^k\frac{\partial \xi_1}{\partial x}+f_2^k\frac{\partial \xi_2}{\partial x}+f_3^k\frac{\partial \xi_3}{\partial x}-f_4^k\left(\frac{\partial \xi_1}{\partial x}+\frac{\partial \xi_2}{\partial x}+\frac{\partial \xi_3}{\partial x}\right),$$
$$\frac{\partial f^k}{\partial y}=f_1^k\frac{\partial \xi_1}{\partial y}+f_2^k\frac{\partial \xi_2}{\partial y}+f_3^k\frac{\partial \xi_3}{\partial y}-f_4^k\left(\frac{\partial \xi_1}{\partial y}+\frac{\partial \xi_2}{\partial y}+\frac{\partial \xi_3}{\partial y}\right), \tag{38}$$
$$\frac{\partial f^k}{\partial z}=f_1^k\frac{\partial \xi_1}{\partial z}+f_2^k\frac{\partial \xi_2}{\partial z}+f_3^k\frac{\partial \xi_3}{\partial z}-f_4^k\left(\frac{\partial \xi_1}{\partial z}+\frac{\partial \xi_2}{\partial z}+\frac{\partial \xi_3}{\partial z}\right).$$

Taking the derivative of local coordinates in Eq. (36) with respect to x, y, and z, we get

$$\frac{\partial \xi_1}{\partial x}=-\frac{1}{3V^k}A_{1x},\frac{\partial \xi_1}{\partial y}=-\frac{1}{3V^k}A_{1y},\frac{\partial \xi_1}{\partial z}=-\frac{1}{3V^k}A_{1z},$$
$$\frac{\partial \xi_2}{\partial x}=-\frac{1}{3V^k}A_{2x},\frac{\partial \xi_2}{\partial y}=-\frac{1}{3V^k}A_{2y},\frac{\partial \xi_2}{\partial z}=-\frac{1}{3V^k}A_{2z}, \tag{39}$$
$$\frac{\partial \xi_3}{\partial x}=-\frac{1}{3V^k}A_{3x},\frac{\partial \xi_3}{\partial y}=-\frac{1}{3V^k}A_{3y},\frac{\partial \xi_3}{\partial z}=-\frac{1}{3V^k}A_{3z}.$$

Then, the substitution of Eq. (39) into Eq. (38) gives

$$\frac{\partial f^k}{\partial x}=-\frac{1}{3V^k}\left\{A_{1x}f_1^k+A_{2x}f_2^k+A_{3x}f_3^k-(A_{1x}+A_{2x}+A_{3x})f_4^k\right\},$$
$$\frac{\partial f^k}{\partial y}=-\frac{1}{3V^k}\left\{A_{1y}f_1^k+A_{2y}f_2^k+A_{3y}f_3^k-(A_{1y}+A_{2y}+A_{3y})f_4^k\right\},$$
$$\frac{\partial f^k}{\partial z}=-\frac{1}{3V^k}\left\{A_{1z}f_1^k+A_{2z}f_2^k+A_{3z}f_3^k-(A_{1z}+A_{2z}+A_{3z})f_4^k\right\}. \tag{40}$$

Now, we obtain the final form of the net current correction term (*i.e.*, Eq. (21)) by substituting Eq. (40) into Eqs. (27) and (30), which gives

$$\vec{F}_{1,2}^{k,ef}\cdot\vec{A}_{1,2}^{k,ef}=\frac{1}{432}\left[\begin{array}{l} w_2\left[\begin{array}{l}\left\{22\left|\vec{A}_2^k\right|+\frac{24D^k}{V^k}\left(\vec{A}_2^k\cdot\vec{A}_1^k\right)\right\}f_1^k+\left\{\frac{24D^k}{V^k}\left(\vec{A}_2^k\cdot\vec{A}_2^k\right)\right\}f_2^k\\ +\left\{7\left|\vec{A}_2^k\right|+\frac{24D^k}{V^k}\left(\vec{A}_2^k\cdot\vec{A}_3^k\right)\right\}f_3^k+\left\{7\left|\vec{A}_2^k\right|+\frac{24D^k}{V^k}\left(\vec{A}_2^k\cdot\vec{A}_4^k\right)\right\}f_4^k\end{array}\right]\\ -v_2\left[\begin{array}{l}\left|\vec{A}_2^k\right|\left\{22f_{\alpha'}^{k'(1,2)}+7f_{\gamma'}^{k'(1,2)}+f_{\delta'}^{k'(1,2)}\right\}\\ -\frac{24D^{k'(1,2)}}{V^{k'(1,2)}}\left\{\begin{array}{l}\left(\vec{A}_2^k\cdot\vec{A}_1^{k'(1,2)}\right)f_1^{k'(1,2)}+\left(\vec{A}_2^k\cdot\vec{A}_2^{k'(1,2)}\right)f_2^{k'(1,2)}\\ +\left(\vec{A}_2^k\cdot\vec{A}_3^{k'(1,2)}\right)f_3^{k'(1,2)}+\left(\vec{A}_2^k\cdot\vec{A}_4^{k'(1,2)}\right)f_4^{k'(1,2)}\end{array}\right\}\end{array}\right]\end{array}\right]. \tag{41}$$

Similarly, the net current correction term over the interface between subcell 1 and subcell 2 can be derived as given by

$$\vec{F}_{1,2}^{k,if}\cdot\vec{A}_{1,2}^{k,if}=\frac{D^k}{36V^k}\left\{\left(\vec{A}_2^k-\vec{A}_1^k\right)\cdot\left(\vec{A}_1^kf_1^k+\vec{A}_2^kf_2^k+\vec{A}_3^kf_3^k+\vec{A}_4^kf_4^k\right)\right\}. \tag{42}$$

The above procedure can be applied to the other external and internal subfaces of subcell 1, and the substitutions of all the results into Eq. (20) gives the final balance equation over subcell 1 (*i.e.*, the DSA equation), which is given by

$$\begin{aligned}&\left[\begin{array}{l}22\left(w_2\left|\vec{A}_2^k\right|+w_3\left|\vec{A}_3^k\right|+w_4\left|\vec{A}_4^k\right|\right)\\ +\frac{24D^k}{V^k}\left\{w_2\left(\vec{A}_2^k\cdot\vec{A}_1^k\right)+w_3\left(\vec{A}_3^k\cdot\vec{A}_1^k\right)+w_4\left(\vec{A}_4^k\cdot\vec{A}_1^k\right)+2\left(\vec{A}_1^k\cdot\vec{A}_1^k\right)\right\}+225\sigma_a^kV_{sc1}^k\end{array}\right]f_1^k\\ &+\left[7\left(w_3\left|\vec{A}_3^k\right|+w_4\left|\vec{A}_4^k\right|\right)+\frac{24D^k}{V^k}\left\{w_2\left(\vec{A}_2^k\cdot\vec{A}_2^k\right)+w_3\left(\vec{A}_3^k\cdot\vec{A}_2^k\right)+w_4\left(\vec{A}_4^k\cdot\vec{A}_2^k\right)+2\left(\vec{A}_1^k\cdot\vec{A}_2^k\right)\right\}+69\sigma_a^kV_{sc1}^k\right]f_2^k\\ &+\left[7\left(w_2\left|\vec{A}_2^k\right|+w_4\left|\vec{A}_4^k\right|\right)+\frac{24D^k}{V^k}\left\{w_2\left(\vec{A}_2^k\cdot\vec{A}_3^k\right)+w_3\left(\vec{A}_3^k\cdot\vec{A}_3^k\right)+w_4\left(\vec{A}_4^k\cdot\vec{A}_3^k\right)+2\left(\vec{A}_1^k\cdot\vec{A}_3^k\right)\right\}+69\sigma_a^kV_{sc1}^k\right]f_3^k\\ &+\left[7\left(w_2\left|\vec{A}_2^k\right|+w_3\left|\vec{A}_3^k\right|\right)+\frac{24D^k}{V^k}\left\{w_2\left(\vec{A}_2^k\cdot\vec{A}_4^k\right)+w_3\left(\vec{A}_3^k\cdot\vec{A}_4^k\right)+w_4\left(\vec{A}_4^k\cdot\vec{A}_4^k\right)+2\left(\vec{A}_1^k\cdot\vec{A}_4^k\right)\right\}+69\sigma_a^kV_{sc1}^k\right]f_4^k\\ &=V_{sc1}^k\left\{225q_1^k+69\left(q_2^k+q_3^k+q_4^k\right)\right\}+\sum_{j=2}^{4}\Theta_j,\end{aligned} \tag{43}$$

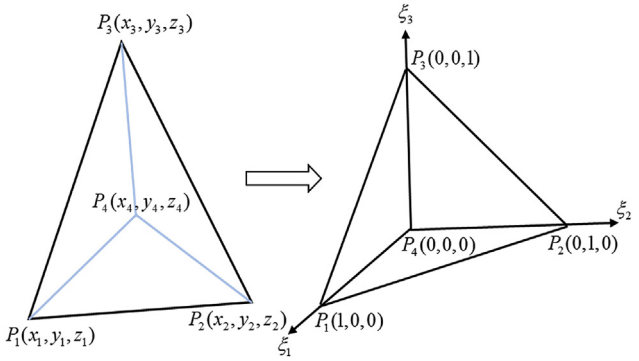

Fig. 2. Barycentric coordinates transformation.

where the term Θ_j is defined by

$$\Theta_j = \left|\vec{A}_j^k\right|\left\{22f_{\alpha'}^{k'(j),(p')} + 7f_{\gamma'}^{k'(j),(p')} + f_{\delta'}^{k'(j),(p')}\right\} - \tilde{D}^{k'(j)}\left\{\sum_{j'=1}^{4}\left(\vec{A}_j^k \cdot \vec{A}_{j'}^{k'(j)}\right)f_{j'}^{k'(j),(p')}\right\}, \tag{44}$$

where $\tilde{D}^{k'(j)}$ is $24D^{k'(j)}/V^{k'(j)}$ and $D^{k'(j)}$ is $1/3\sigma_t^{k'(j)}$.

The remaining discretized diffusion equations for the other three subcells in the tetrahedral mesh k can be derived in the same manner. Actually, the discretized equations represent a discontinuous linear discretization of the diffusion equation, and we solve them using a GS-like iteration, which is represented by the iteration index (p) in Eqs. (43) and (44). The mesh index $k'(j)$ represents the neighboring mesh opposite to the face j of mesh k of subcell 1. Also, it should be noted that the iteration index (p') in Eq. (44) for DSA depends on the meshes. That is to say, the iteration index (p') becomes $(p+1/2)$ if the mesh $k'(j)$ has already been swept; otherwise, it becomes (p). The index $(p+1/2)$ without acceleration is the same as $(p+1)$. The convergence of the GS-like iteration may depend on the order of the cell sweep (called diffusion sweep in this work). At present, we used the same order of cell sweep for the GS-like iteration as that used for the transport sweep.

The coupling procedure of transport equation with DSA is explained as follows:

i. The LDEM-SCB(1) equations (*i.e.,* Eq. (12)) are solved with a transport sweep and with the previous scalar flux iterate, *i.e.,* $\phi^{(\ell)}$. Then, the scalar flux $\phi^{(\ell+1/2)}$ is calculated by using the angular flux $\psi^{(\ell+1/2)}$ obtained from the transport sweep.
ii. The source term of the diffusion equation (*i.e.,* the first equation of Eq. (16)) is calculated using $\phi^{(\ell)}$ and $\phi^{(\ell+1/2)}$.
iii. The discretized diffusion equations (*i.e.,* Eq. (43) and the others for three subcells) are solved, which give the scalar flux correction, $f^{(\ell+1)}$.
iv. The next scalar flux iterate (*i.e.,* $\phi^{(\ell+1)}$) is calculated by adding $\phi^{(\ell+1/2)}$ to the scalar flux correction $f^{(\ell+1)}$.

$$\phi^{(\ell+1)} = \phi^{(\ell+1/2)} + f^{(\ell+1)}. \tag{45}$$

v. The scattering source of LDEM-SCB(1) is updated using the new scalar flux.
vi. This procedure is repeated until the scalar fluxes are converged with a prescribed convergence criterion.

2.3. Derivation of FMR equations

The rebalance method is one of the earliest acceleration methods used in the neutron transport problems and it has been widely used due to its simple and easy implementation. In transport calculations, the rebalance method couples the high-order (*i.e.,* the discretized transport equation) to the low-order calculations. The lower-order equations are derived using the balance equation over a fine mesh or a coarse mesh (*i.e.,* a group of fine meshes) [18–22].

In this work, we suggest a linear FMR method to accelerate the DSA equation. The rebalance schemes are usually applied to the neutron transport equations, while this linear FMR method is applied to the diffusion equation. The derivation of the FMR equation starts with the balance equation, which is just obtained by integrating Eq. (14) over a tetrahedral mesh k. That is to say, the next iterate of the GS-like iteration of the DSA equation is required to satisfy the following balance equation over a tetrahedral mesh k.

$$\int_{A^k} dA\left(\vec{F}^{k,(p+1)} \cdot \hat{n}\right) + \sigma_a^k \bar{f}^{k,(p+1)} V^k = \bar{q}^k V^k. \tag{46}$$

However, we will omit the iteration index $(p+1)$ of the GS-like iteration for simplicity. The surface bounding the tetrahedron is divided into four external surfaces as:

$$\vec{F}_1^k \cdot \vec{A}_1^k + \vec{F}_2^k \cdot \vec{A}_2^k + \vec{F}_3^k \cdot \vec{A}_3^k + \vec{F}_4^k \cdot \vec{A}_4^k + \sigma_a^k \bar{f}^k V^k = \bar{q}^k V^k. \tag{47}$$

The net current correction vector $\vec{F}_j^k$ over an external face j is split into the incoming and outgoing partial current corrections as follows:

$$\vec{F}_j^k \cdot \vec{A}_j^k = \left|\vec{A}_j^k\right|\left(\vec{F}_j^k \cdot \hat{n}_j^k\right) = \left|\vec{A}_j^k\right|\left(w_j F_j^{k,+} - v_j F_{j'}^{k'(j),+}\right), \tag{48}$$

where w_j and v_j are boundary conditions on the external face $\vec{A}_j^k$. The outgoing $F_j^{k,+}$ and the incoming $F_{j'}^{k'(j),+}$ partial current corrections can be derived using a similar procedure used in the derivation of the DSA equations as follows:

$$F_j^{k,+} = \frac{1}{12}\left(f_\alpha^k + f_\beta^k + f_\gamma^k\right) + \frac{D^k}{6V^k\left|\vec{A}_j^k\right|}\left\{\begin{array}{l}\left(\vec{A}_j^k \cdot \vec{A}_1^k\right)f_1^k + \left(\vec{A}_j^k \cdot \vec{A}_2^k\right)f_2^k \\ +\left(\vec{A}_j^k \cdot \vec{A}_3^k\right)f_3^k + \left(\vec{A}_j^k \cdot \vec{A}_4^k\right)f_4^k\end{array}\right\}, \tag{49}$$

$$F_{j'}^{k'(j),+} = \frac{1}{12}\left(f_{\alpha'}^{k'(j)} + f_{\beta'}^{k'(j)} + f_{\gamma'}^{k'(j)}\right) - \frac{D^{k'(j)}}{6V^{k'(j)}\left|\vec{A}_j^k\right|}\left\{\begin{array}{l}\left(\vec{A}_j^k \cdot \vec{A}_1^{k'(j)}\right)f_1^{k'(j)} + \left(\vec{A}_j^k \cdot \vec{A}_2^{k'(j)}\right)f_2^{k'(j)} \\ +\left(\vec{A}_j^k \cdot \vec{A}_3^{k'(j)}\right)f_3^{k'(j)} + \left(\vec{A}_j^k \cdot \vec{A}_4^{k'(j)}\right)f_4^{k'(j)}\end{array}\right\}. \tag{50}$$

In Eqs. (49) and (50), α, β and γ represent the node indices on face j of mesh k, whereas α', β' and γ' represent the node indices on face j' of the mesh $k'(j)$, respectively. The net current correction vectors across the other external faces can be similarly derived and the substitution of them into Eq. (47) gives the following balance

equation over the tetrahedral mesh k:

$$\sum_{j=1}^{4} T_j^k f_j^k - \sum_{j=1}^{4} v_j \zeta_j^k = 3V^k \left(q_{sc1}^k + q_{sc2}^k + q_{sc3}^k + q_{sc4}^k \right), \tag{51}$$

where the terms T_j^k and ζ_j^k are defined by

$$T_j^k = \left\{ 3\sigma_a^k V^k + \sum_{\substack{i=1 \\ i \neq j}}^{4} w_i \left| \vec{A}_i^k \right| + \frac{\tilde{D}^k}{12} \sum_{i=1}^{4} w_i \left(\vec{A}_i^k \cdot \vec{A}_j^k \right) \right\}, \tag{52}$$

$$\zeta_j^k = \left\{ \left| \vec{A}_j^k \right| \left(f_{\alpha'}^{k'(j)} + f_{\beta'}^{k'(j)} + f_{\gamma'}^{k'(j)} \right) - \frac{\tilde{D}^{k'(j)}}{12} \sum_{j'=1}^{4} \left(\vec{A}_j^k \cdot \vec{A}_{j'}^{k'(j)} \right) f_{j'}^{k'(j)} \right\}. \tag{53}$$

The same equation (*i.e.*, Eq. (51)) can also be obtained by simply adding the DSA equations of all the four subcells in a tetrahedral mesh, which shows that both the DSA method and the FMR method discretizations are based on the neutron balance equation. For the linear FMR, we define an additive rebalance factor $\gamma^{k,(p+1)}$ for the scalar flux correction as follows:

$$f_j^{k,(p+1)} = f_j^{k,(p+1/2)} + \gamma^{k,(p+1)}. \tag{54}$$

Finally, the substitution of Eq. (54) into Eq. (51) gives the following final linear rebalance equation over mesh k:

$$3\left\{ \sum_{j=1}^{4} \left(w_j \left| \vec{A}_j^k \right| \right) + 4\sigma_a^k V^k \right\} \gamma^{k,(p+1)} - 3\sum_{j=1}^{4} \left(v_j \left| \vec{A}_j^k \right| \gamma^{k'(j),(p+1)} \right) = 12\bar{q}^k V^k - \sum_{j=1}^{4} T_j^k f_j^{k,(p+1/2)} + \sum_{j=1}^{4} \zeta_j^{k,(p+1/2)}, \tag{55}$$

where $\gamma^{k'(j),(p+1)}$ is a rebalance factor for the neighboring mesh $k'(j)$. These equations can be written in the following matrix form:

$$\mathbf{A}\vec{\gamma} = \vec{\mathbf{b}}, \tag{56}$$

where $\vec{\mathbf{b}}$ is the collection of the right-hand sides of Eq. (55).

The rebalance equations (*i.e.*, Eq. (55)) constitute a system of linear equations whose matrix is symmetric positive definite, so the CG method can be applied for solving them. The fact that the matrix **A** is symmetric can be deduced from the symmetry of the coupling coefficients between the four adjacent meshes in the rebalance equation. The positive definiteness of the matrix **A** is based on the fact that it is symmetric and has diagonal dominance with positive diagonal elements [17].

In this work, we considered two different preconditioners to CG for improving the overall efficiency of DSA(FMR), *i.e.*, the Jacobi and the split preconditioners. The Jacobi preconditioner is the diagonal matrix **D** of the symmetric positive definite system of equations (*i.e.*, formed by the first term of the left-hand side of Eq. (55)), and it is very easy to implement. It needs only to re-calculate the residual $\vec{z}_i = \mathbf{D}_{ii}^{-1} \vec{r}_i$ of the preconditioned system, where r_i is the *i'th* component of the residual of CG. The split preconditioner is the

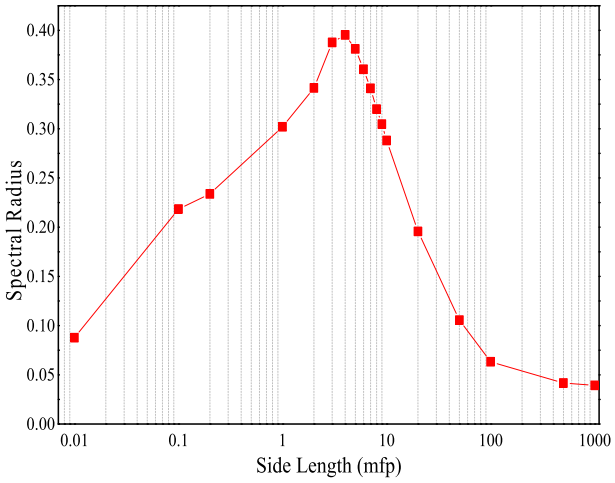

Fig. 3. Spectral radius as a function of side length of the unit box for the first test problem.

matrix $\mathbf{M} = LL^T$, where L is the lower triangular matrix of the original matrix **A** given in Eq. (56). The first term of the left-hand side of Eq. (55) is the diagonal element, and the second term represents the off-diagonal elements of the matrix **A**. The off-diagonal elements represent the couplings with the four adjacent meshes. Therefore, the split preconditioner is more costly than the Jacobi preconditioner for each CG iteration. The detailed algorithm of the split preconditioned conjugate gradient (SCG) is as follows [17]:

First, we compute the vectors:

$$\vec{r}_0 := \vec{\mathbf{b}} - \mathbf{A}\vec{\gamma}_0;\ \vec{u}_0 = L^{-1}\vec{r}_0;\ \text{and}\ \vec{p}_0 = \left(L^T\right)^{-1}\vec{u}_0. \tag{57}$$

Then, for $i = 0, 1, \ldots$ until convergence:

$$\begin{aligned} \omega_i &:= \frac{(\vec{u}_i, \vec{u}_i)}{(\mathbf{A}\vec{p}_i, \vec{p}_i)}, \\ \vec{\gamma}_{i+1} &:= \vec{\gamma}_i + \omega_i \vec{p}_i, \\ \vec{u}_{i+1} &:= \vec{u}_i - \omega_i L^{-1}\mathbf{A}\vec{p}_i, \\ v_i &:= \frac{(\vec{u}_{i+1}, \vec{u}_{i+1})}{(\vec{u}_i, \vec{u}_i)}, \\ \vec{p}_{i+1} &:= \left(L^T\right)^{-1}\vec{u}_{i+1} + v_i \vec{p}_i. \end{aligned} \tag{58}$$

This algorithm is solved for a specified convergence criterion. In this algorithm, the vectors $L^{-1}\vec{r}_0$ and $L^{-1}\mathbf{A}\vec{p}_i$ are calculated with the forward substitution, while $(L^T)^{-1}\vec{u}_0$ and $(L^T)^{-1}\vec{u}_{i+1}$ are calculated with the backward substitution.

The calculation procedure for FMR is described in accordance with the one for DSA, which is explained as follows:

i. The scalar flux corrections $f_j^{k,(p+1/2)}$ from the DSA sweep are used in the right-hand side of the FMR equations (*i.e.*, Eq. (55)).
ii. The FMR diffusion equations are solved by the preconditioned CG method to calculate the rebalance factors $\gamma^{k,(p+1)}$ (*i.e.*, Eq. (58)).
iii. The scalar flux corrections are updated and then used in the DSA diffusion equations as follows:

$$f_j^{k,(p+1)} = f_j^{k,(p+1/2)} + \gamma^{k,(p+1)}. \quad (59)$$

iv. This cycle is repeated until the diffusion equation for DSA converges.
v. The scalar flux is then updated once DSA is converged,

$$\phi_j^{k,(\ell+1)} = \phi_j^{k,(\ell+1/2)} + f_j^{k,(p+1)}, \quad (60)$$

which replaces Eq. (45).

Recently, we have performed Fourier analysis of the GS-like iteration for the discretized DSA equation and its FMR acceleration to understand their convergence characteristics [23].

3. Numerical tests and results

The DSA method was applied to several test problems to show its effectiveness. Because the theoretical work using the Fourier analysis has not been performed, numerical estimates of the spectral radius were used to measure the convergence of the source iteration coupled with the DSA method. The numerical estimate of the spectral radius is made using

$$\rho \approx \frac{\left\| \vec{\phi}^{(\ell+1)} - \vec{\phi}^{(\ell)} \right\|_2}{\left\| \vec{\phi}^{(\ell)} - \vec{\phi}^{(\ell-1)} \right\|_2}, \quad (61)$$

where $\|\|_2$ means the L_2 norm of the vector.

The first test problem is a one group homogeneous problem consisting of a 10 × 10 × 10 grid of identical boxes called unit box, and it has a uniform source of 10 neutrons $cm^{-3}sec^{-1}$. This problem is similar to the one considered in Ref. 11. The side length of each unit box is 2.0 cm, and each unit box is divided into six tetrahedral meshes. We used two azimuthal and two polar angles per octant with the Chebyshev-Legendre quadrature, wherein the reflective boundary conditions are applied to the -*x*, -*y*, and -*z* direction external faces, while the vacuum boundary conditions are applied to all other external faces. The scattering ratio was fixed to 0.9999, but the total cross-section was varied to show the effect of the mesh size in terms of mean free path (mfp). The convergence criteria for the source iteration (SI) and DSA are 1.0×10^{-10} and 1.0×10^{-8}, respectively. We used the pointwise convergence criteria both for the source iteration and DSA, which are defined as

$$\max_i \left| \frac{\vec{\phi}_i^{(\ell+1)} - \vec{\phi}_i^{(\ell)}}{\vec{\phi}_i^{(\ell+1)}} \right| \le \begin{bmatrix} 10^{-10} for\ SI \\ 10^{-8} for\ DSA \end{bmatrix}. \quad (62)$$

The numerical estimates of the spectral radii are plotted in Fig. 3 as a function of the side length of the unit box (mfp). This figure shows that our DSA converges very fast over a wide range of side lengths (mfp), and the spectral radii are less than 0.40. However, it should be noted that the spectral radii for the small mesh sizes (e.g., 0.01 mfp) is smaller than the fine mesh limit (i.e., ~0.227*c*, *c* is the scattering-to-total ratio) of Fourier analysis because the problem size along one direction for 0.01 mfp mesh size is 0.1 mfp, which leads to neutron leakage.

The second test problem is considered to show the effects of the minimum aspect ratio of tetrahedral meshes on the convergence of the DSA method [11]. The minimum aspect ratio (α_{min}) is defined as the ratio of three times the radius of the inscribed circle to the radius of the circumscribed circle. This homogeneous problem consisted of an 8 × 8 × 8 grid of unit boxes. The total cross-section is 3.5 cm^{-1}, and the scattering ratio is 0.9999. The boundary conditions are the same as that of the previous test problem. Table 1 shows various tetrahedral meshes having different minimum aspect ratios [11].

Table 1
Minimum aspect ratios and side lengths of unit boxes for the second test problem.

#	α_{min}	h_x (*cm*)	h_y (*cm*)	h_z (*cm*)
I	0.632	1.0	1.0	1.0
II	0.562	2.0	2.0	3.0
III	0.487	1.0	1.0	2.0
IV	0.421	2.0	2.0	5.0
V	0.370	2.0	1.0	3.0
VI	0.327	3.0	1.0	3.0
VII	0.256	2.0	1.0	5.0
VIII	0.170	2.0	1.0	8.0
IX	0.116	8.0	1.0	10.0

The results of our DSA method are compared to those of other DSA methods such as FCDSA (Fully Consistent DSA) [11], WLA DSA (Wareing, Larsen and Adams' DSA) [13] and M4S DSA (Modified Four-Step DSA) [9] even if they are applied to DFEM. The FCDSA method is derived in a fully consistent way by discretizing the P_1 equations and the transport equation with the isoparametric linear discontinuous finite elements. On the other hand, the discretized diffusion equations in the WLA DSA method are derived by taking the asymptotic diffusion limit of the discretized transport equations [7]. The M4S DSA method is the modified four-step method to make an approximation in the first moment equations that arise in the full four-step procedure. For example, Adams and Martin [9] derived DSA equations for DFEM by discretizing the continuous diffusion equation with a similar way (but not consistent in usual sense to the discretized DFEM transport equations) used in DFEM and replacing the net current correction with their upstream partial current corrections.

The numerical estimates of the spectral radii obtained from our DSA method for this problem are compared with those obtained from other DSA methods [11] as shown in Fig. 4. Our DSA method for LDEM-SCB(1) shows considerably smaller spectral radii than those of WLA DSA and M4S DSA schemes, but higher ones than those of FCDSA. Also, it is noted in Fig. 4 that the spectral radii of our DSA and FCDSA methods show only small changes over different minimum aspect ratios.

The third test problem is a one group homogeneous problem consisting of a 30 × 30 × 30 grid of unit boxes having a uniform

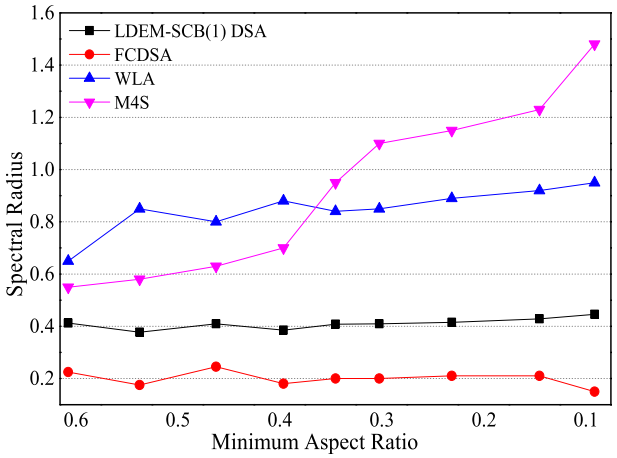

Fig. 4. Spectral radius versus minimum aspect ratio for different DSA methods for the second test problem.

source of 10 neutrons $cm^{-3}sec^{-1}$. The side length of each unit box is 1.0 cm. The boundary conditions are the same as those of previous test problems. For this problem, the pointwise convergence criteria for the source iteration of the transport, the DSA, and the FMR equations are 1.0×10^{-8}, 1.0×10^{-5}, and 1.0×10^{-2}, respectively. We used the following convergence criterion on the relative residual for FMR with a conjugate gradient method:

$$\frac{\left\|\vec{r}^{(\ell)}\right\|_2}{\left\|\vec{r}^{(0)}\right\|_2} \leq 10^{-2}, \tag{63}$$

where the residual $\vec{r}^{(\ell)}$ is defined as

$$\vec{r}^{(\ell)} = \vec{\mathbf{b}} - \mathbf{A}\vec{\gamma}. \tag{64}$$

We considered five different cases having different total cross-sections with a fixed scattering ratio of 0.9999, and the results are summarized in Table 2. In this test problem, the Jacobi preconditioner and the split preconditioner are applied to the CG method for FMR. The results presented in Table 2 are obtained with DSA(FMR) with the preconditioned CG. This table shows that the DSA method effectively reduces the number of source iterations. In addition, DSA with FMR(CG) even without preconditioning gives significant speedups in computing time, ranging from 9.6 to 27 in comparison with the source iteration. Also, it is shown that FMRs(CG) with the Jacobi and the split preconditioning give much higher speedups ranging from 11.3 to 40.6 than FMR(CG) without preconditioning and that FMR(CG) with the split preconditioner gives higher speedups than the one with the Jacobi preconditioner except for the test Case I.

A comparison of results for this test problem is also presented in Fig. 5, in which the average numbers of CG iterations per DSA sweep are plotted for CG, JCG (CG with Jacobi preconditioner) and SCG (CG with split preconditioner). From Fig. 5, it is clear that the preconditioned CGs have considerably smaller average numbers of CG iterations per DSA sweep than the unpreconditioned one. In particular, SCG gives a significant reduction in the number of CG iterations than JCG.

Table 3 compares the numbers of DSA sweeps with and without FMR application to DSA after each transport sweep. From this table, it is shown that the FMR method with unpreconditioned CG is very effective in reducing both the number of DSA sweeps and the computing time. In this table, the speedup is defined as the ratio of the computing times between DSA methods with and without FMR. The speedup factor, in this case, shows that the DSA acceleration with the FMR(CG) method is much more effective than the DSA without the FMR method. In particular, the numbers of DSA sweeps are drastically reduced with FMR. The numbers of DSA sweeps with FMR are decreased by the factors of a few tens to several hundred in comparison with DSA without FMR. The numerical estimates of the spectral radii are also given in this table, and they slightly increase as the total cross-section increases, but they are less than 0.38.

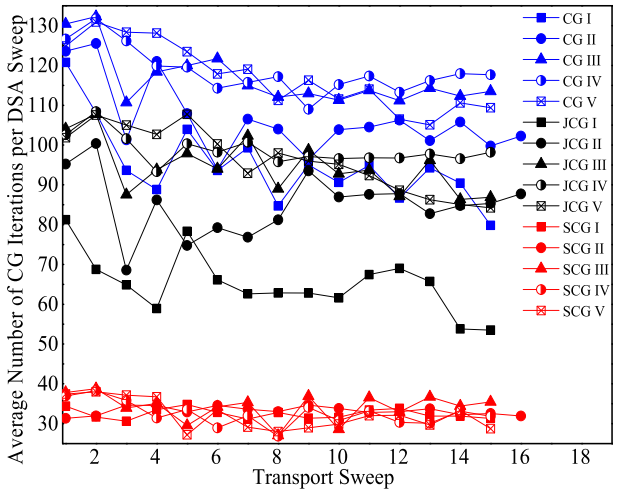

Fig. 5. Average numbers of CG iterations per DSA sweep for the third test problem.

The last test problem is a heterogeneous cube of outer dimensions 50 cm × 50 cm × 50 cm in which four cylinders, each having 10 cm diameter and 50 cm height, are embedded with equal distances. The configuration of this problem is shown in Fig. 6. The distance between two adjacent cylinders is 10 cm. This problem is considered to test the practical applicability of the DSA method with FMR by checking whether it still has significant speedups for a realistic heterogeneous problem. We used four azimuthal and four polar angles per octant with the Chebyshev-Legendre quadrature and vacuum boundary conditions on all the external sides. In this test problem, the cube outside the cylinders has a total cross-section of 1.0 cm^{-1}, a scattering cross-section of 0.999 cm^{-1}, and 1 neutron $cm^{-3}sec^{-1}$ source strength, while the four cylinders have variable cross-sections as shown in Table 4 and the source strength is 10 neutrons $cm^{-3}sec^{-1}$. Actually, we considered fifteen different cases having five different total cross-sections with three different scattering-to-total cross-section ratios. For this problem 60,560 tetrahedral meshes, 10,927 nodes and 122,688 faces are generated as shown in Fig. 6.

Fig. 7 shows the scalar flux distribution for Case XII for this test problem. Fig. 7 shows that there are very steep gradients in the region between the outer cube and the cylinders due to the differences in the cross-sections and the source strengths.

The source iteration is accelerated with DSA(FMR) coupled with CG, JCG, and SCG. The effectiveness of the preconditioners applied to CG in the heterogeneous medium is compared in terms of the number of CG iterations per DSA sweep at different values of the scattering ratio as shown in Figs. 8–10. From these figures, it is

Table 2
Comparison of DSA(FMR) speedups for the third test problem.

Test Case	Total Cross-Section (cm^{-1})	Source Iteration without DSA (without FMR)		Source Iteration with DSA (without FMR)		Source Iteration with DSA (with FMR)			Source Iteration Speedup			
		Number of Iterations	SI Time (hours)	Number of Iterations	SI Time (hours)	SI(DSA)+ FMR(CG) Time (hours)	SI(DSA)+ FMR(JCG) Time (hours)	SI(DSA)+ FMR(SCG) Time (hours)	SI(DSA)	SI(DSA)+ FMR(CG)	SI(DSA)+ FMR(JCG)	SI(DSA)+ FMR(SCG)
I	1.0	4698	5.033	15	2.783	0.523	0.371	0.446	1.81	9.62	13.6	11.3
II	1.5	9367	9.167	16	6.347	0.542	0.377	0.352	1.44	16.9	24.3	26.0
III	2.0	14936	14.47	15	7.78	0.697	0.608	0.504	1.86	20.8	23.8	28.7
IV	2.5	20982	20.81	15	9.854	0.77	0.737	0.512	2.11	27.0	28.3	40.6
V	3.0	27161	26.93	15	10.401	1.049	0.821	0.671	2.59	25.7	32.8	40.1

Table 3
Comparison of numbers of DSA sweeps with and without FMR coupled with DSA for the third test problem.

Number of Transport Sweeps	Case I		Case II		Case III		Case IV		Case V	
	Number of DSA Sweeps w/o FMR	Number of DSA Sweeps with FMR	Number of DSA Sweeps w/o FMR	Number of DSA Sweeps with FMR	Number of DSA Sweeps w/o FMR	Number of DSA Sweeps with FMR	Number of DSA Sweeps w/o FMR	Number of DSA Sweeps with FMR	Number of DSA Sweeps w/o FMR	Number of DSA Sweeps with FMR
1	766	31	827	17	875	24	897	24	903	29
2	3660	52	3785	38	3165	51	2443	67	2144	81
3	11280	26	15446	14	19888	15	2291	20	18350	28
4	918	41	2516	26	8596	30	10094	36	15197	58
5	1944	26	1905	13	17515	35	24415	55	24176	67
6	9893	26	16591	25	2651	38	9451	39	12154	51
7	1578	31	3918	27	15279	53	22103	36	20724	43
8	452	27	547	24	12870	32	21342	39	14209	45
9	10145	25	11582	25	12768	48	18191	40	19922	45
10	2710	23	10869	22	14445	32	15808	39	18661	44
11	412	24	12800	26	13631	49	13934	42	14179	51
12	9985	26	10960	25	17281	33	15085	38	19504	50
13	2477	29	11027	23	11225	49	17350	46	18841	57
14	2012	32	9215	24	13728	38	13505	46	20927	56
15	3728	35	7593	21	13551	41	16646	45	16783	58
16	–	–	8529	23	–	–	–	–	–	–
Time (hours)	2.783	0.523	6.347	0.542	7.7803	0.697	9.8544	0.77	10.4086	1.049
Spectral radius	0.2927		0.2988		0.3348		0.3359		0.3732	
Speedup	5.3		11.7		11.2		12.8		9.9	

shown that the preconditioned CGs are very effective for all the cases having different cross-sections. In particular, the SCG is much more effective than CG and JCG. As the scattering ratio increases, the number of CG iterations per DSA sweep also increases. This effect is more evident in CG than that of JCG and SCG. However, this effect on SCG is very small as shown in Figs. 8–10. It shows that the split preconditioner is very effective in reducing the inner iterations of the CG method.

The results for these test cases are also presented in Table 5 to show a comparison of the speedups in the computing time of the DSA(FMR) method coupled with CG, JCG, and SCG. From the table, it is shown that DSA(FMR) is very effective even in the heterogeneous test problem, and the speedups are improved by the preconditioned CGs for this heterogeneous problem. However, by comparing the speedups of DSA and DSA(FMR) without preconditioner, it is observed that the difference in the speedups gradually decreases with the increasing mean free path. For example, for Case XV the DSA(FMR) without preconditioner becomes slower than DSA. That is to say, FMR with unpreconditioned CG gives no speedup to DSA but slightly degrades the speedup from 10.1 to 9.76. It is because of higher computing time of CG. For the same case, JCG and SCG give better speedups of 25.27 and 21.72, respectively, whereas CG becomes ineffective as compared to DSA. It shows that the preconditioners are very effective for all the cases. However, it is noted that JCG is slightly more effective in terms of speedup than SCG, even though SCG is significantly more effective in reducing the number of CG iterations than JCG. The smaller speedups of SCG than that of JCG are due to the higher computing efforts of SCG for each CG sweep than JCG. This table also shows that the speedups are improved for higher scattering ratios in comparison with the lower scattering ratios.

Next, the effect of preconditioner on the relative residual for the convergence of CG at different scattering ratios is analyzed for Case XV. The relative rate of decrease of the residual to the initial residual during CG iterations is analyzed during only the first source iteration after the last DSA sweep for CG, JCG, and SCG by plotting it on a logarithmic scale. The changes in the relative residual for CG, JCG, and SCG are compared in Fig. 11. For this comparison, the convergence criterion for the CG method is fixed to 1.0×10^{-4}. Fig. 11 shows that SCG and JCG have much faster reductions in the

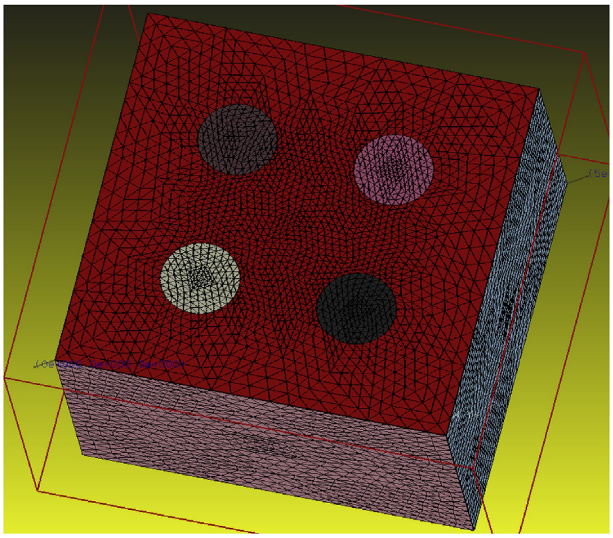

Fig. 6. Geometrical description of heterogeneous test problem.

Table 4
Material specification of cylinders for the heterogeneous test problem.

Test Case	Scattering Ratio	Total Cross-Section (cm^{-1})
Case I	0.9	2.0
Case II	0.99	2.0
Case III	0.999	2.0
Case IV	0.9	3.0
Case V	0.99	3.0
Case VI	0.999	3.0
Case VII	0.9	4.0
Case VIII	0.99	4.0
Case IX	0.999	4.0
Case X	0.9	5.0
Case XI	0.99	5.0
Case XII	0.999	5.0
Case XIII	0.9	10.0
Case XIV	0.99	10.0
Case XV	0.999	10.0

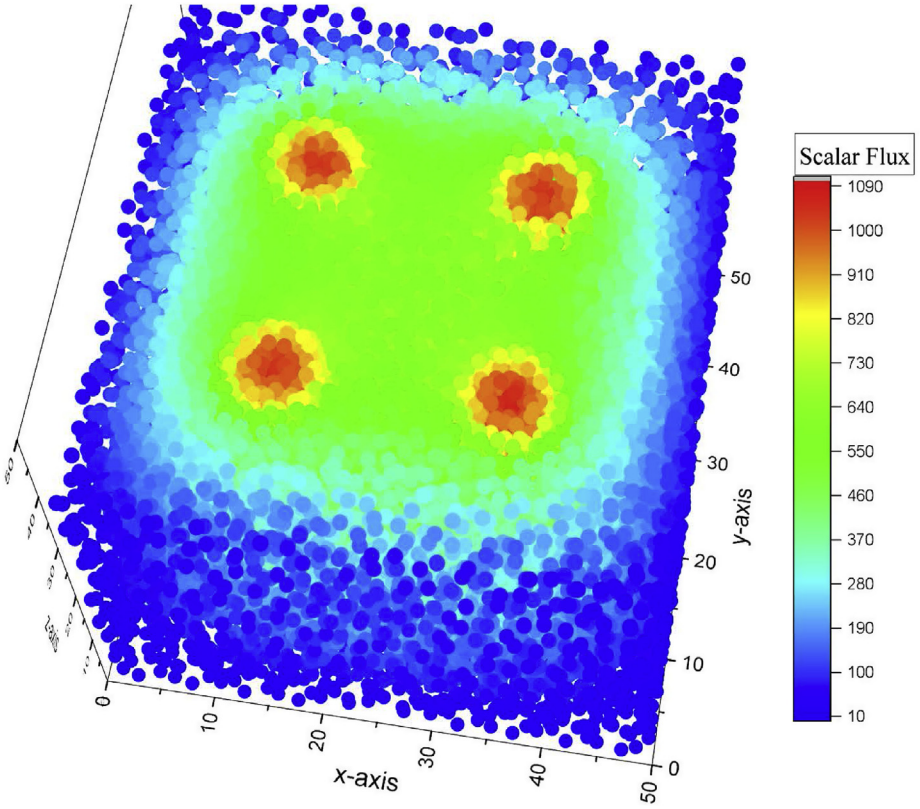

Fig. 7. Scalar flux distribution of Case XII in the heterogeneous test problem.

relative residual than CG without preconditioning and that SCG has a considerably faster reduction rate than JCG. When the scattering ratio increases from 0.9 to 0.999, the number of iterations also increases. However, JCG and SCG show much better performance as compared to CG even for high scattering ratio. It should also be noted that SCG has a much smaller relative residual after the first iteration than that of JCG.

4. Summary and conclusion

In this work, a diffusion synthetic acceleration technique for the S_N transport equation discretized with LDEM-SCB(1) on unstructured tetrahedral meshes was derived by consistently discretizing the continuous diffusion equation with LDEM-SCB(1). The DSA equations were derived by applying the same procedure used in the derivation of LDEM-SCB(1) to the continuous diffusion equation. That is to say, the derivation of the DSA equations used the same subcell balance equations and the same expansion of the flux as those used in the derivation of LDEM-SCB(1). However, the discretized DSA equations are not fully consistent with the LDEM-SCB(1) discretized transport equations. In particular, the net

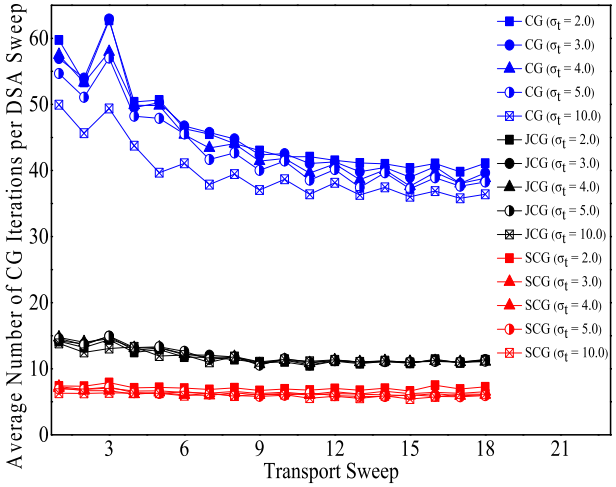

Fig. 8. Comparison of average numbers of CG iterations with different preconditioners (c = 0.9).

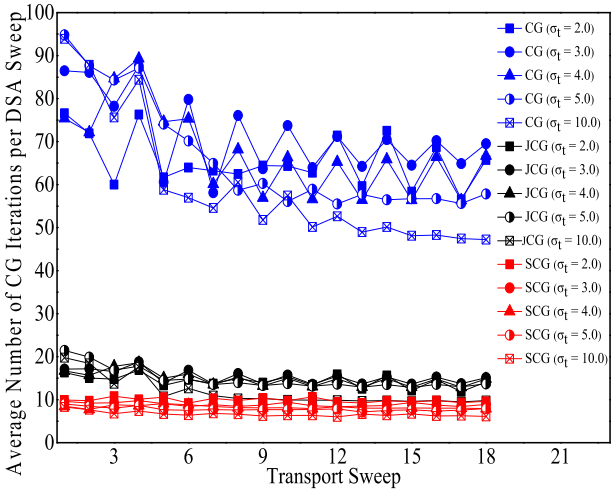

Fig. 9. Comparison of average numbers of CG iterations with different preconditioners (c = 0.99).

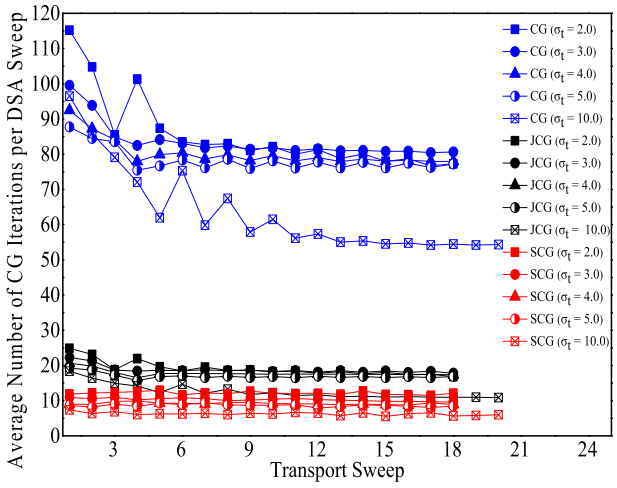

Fig. 10. Comparison of average numbers of CG iterations with different preconditioners (c = 0.999).

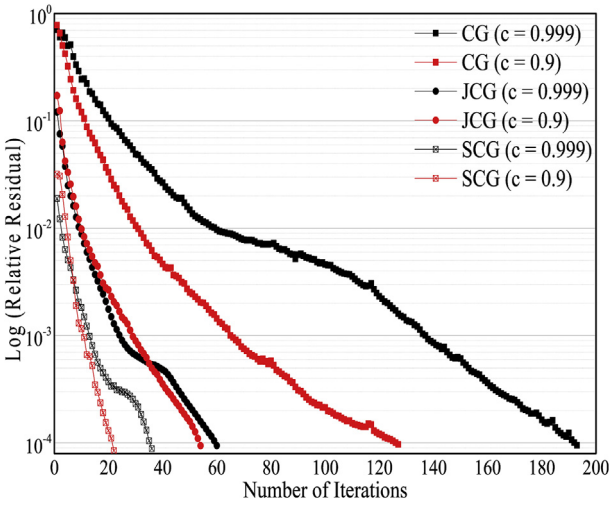

Fig. 11. Effect of preconditioners on the convergence of CG.

current correction terms in the subcell balance equation for the diffusion equation are decomposed into the partial current corrections, and these partial current corrections are represented in terms of scalar flux corrections of the upstream meshes from which the neutrons flow. The detailed derivations of the DSA equations were simplified using the transformation between the barycentric and global coordinates systems. The resulting DSA equations constitute a linear discontinuous diffusion discretization.

The DSA equations can be naturally solved using a GS-like iteration method, but this iterative scheme was shown to be ineffective for large problems having high scattering ratios, which degrades the effectiveness of the DSA method. To overcome this issue, a linear fine mesh rebalance scheme was newly devised based on each tetrahedral mesh and applied to accelerate the GS-like iteration. In particular, the FMR equations constitute a system of linear equations whose matrix is symmetric positive definite and they were solved using the preconditioned CG methods. At present, we considered the Jacobi and split preconditioners for CG.

The DSA method was applied to three homogeneous test problems and one heterogeneous test problem to show its effectiveness in terms of computing time (*i.e.,* speedup), reducing the number of iterations, and the numerical estimate of the spectral radius. From the numerical tests for the homogeneous problems, it was found that our DSA(FMR) method for LDEM-SCB(1) rapidly converges for a wide range of mesh sizes and for various shapes of

Table 5
Comparison of DSA(FMR) speedups for the fourth test problem.

Test Case	Source Iteration without DSA (without FMR)		Source Iteration with DSA (without FMR)			Source Iteration Time with DSA (with FMR)			Source Iteration Speedup			
	Number of Iterations	SI Time (hours)	Spectral Radius	Number of Iterations	SI(DSA) Time (hours)	SI(DSA)+ FMR(CG) Time (hours)	SI(DSA)+ FMR(JCG) Time (hours)	SI(DSA)+ FMR(SCG) Time (hours)	SI(DSA)	SI(DSA)+ FMR(CG)	SI(DSA)+ FMR(JCG)	SI(DSA)+ FMR(SCG)
Case I	1237	2.22	0.3598	18	0.555	0.309	0.163	0.213	4.0	7.19	13.61	10.40
Case II	2161	3.733	0.3617	18	0.873	0.513	0.214	0.247	4.28	7.28	17.41	15.14
Case III	3492	5.696	0.3667	18	1.30	0.692	0.219	0.295	4.38	8.23	26.02	19.29
Case IV	1211	2.227	0.3589	18	0.544	0.316	0.162	0.254	4.10	7.05	13.73	8.750
Case V	2119	3.547	0.3573	18	0.805	0.599	0.221	0.292	4.41	5.92	16.04	12.14
Case VI	4112	6.691	0.3597	18	1.314	0.853	0.288	0.366	5.09	7.84	23.25	18.30
Case VII	1192	2.014	0.3586	18	0.58	0.383	0.163	0.197	3.47	5.27	12.39	10.24
Case VIII	2086	4.139	0.3572	18	0.85	0.654	0.227	0.253	4.87	6.32	18.22	16.39
Case IX	4725	7.908	0.3596	18	1.263	0.944	0.332	0.412	6.26	8.38	23.82	19.21
Case X	1176	1.969	0.3585	18	0.561	0.393	0.163	0.187	3.51	5.01	12.07	10.53
Case XI	2061	3.668	0.3578	18	0.822	0.705	0.244	0.323	4.46	5.2	15.02	11.35
Case XII	5346	8.993	0.3688	18	1.437	1.204	0.401	0.455	6.26	7.47	22.43	19.76
Case XIII	1124	2.319	0.3584	18	0.558	0.304	0.261	0.285	4.15	7.63	8.90	8.140
Case XIV	1979	6.349	0.3629	18	0.794	0.663	0.286	0.339	8.00	9.58	22.17	18.73
Case XV	8029	14.61	0.4384	20	1.448	1.497	0.578	0.673	10.1	9.76	25.27	21.72

tetrahedral meshes. It provides both significant speedups of 10–40 and significant reductions in the number of transport sweeps in comparison with the source iteration. The test of our DSA(FMR) to a heterogeneous test problem showed that DSA(FMR) gives significant speedups up to 9–26 for a realistic heterogeneous problem. Through the numerical tests, it was also found that the FMR method with the preconditioned CG is critical to achieving significant speedups. At present, we did not consider the parallel computation, but this will be pursued in the future to further reduce the computing time.

Acknowledgments

This work was supported by the NRF (National Research Foundation of Korea) through Project No. 2019M2D2A1A02057890.

Appendix A. Supplementary data

Supplementary data to this article can be found online at https://doi.org/10.1016/j.net.2019.08.021.

References

[1] T.A. Wareing, J.M. McGhee, J.E. Morel, S.D. Pautz, Discontinuous finite element S_N methods on three-dimensional unstructured grids, Nucl. Sci. Eng. 138 (2001) 256–268.
[2] J.E. Morel, J.S. Warsa, An S_N spatial discretization scheme for tetrahedral meshes, Nucl. Sci. Eng. 151 (2005) 157–166.
[3] J.S. Warsa, A continuous finite element-based discontinuous finite element method for S_N transport, Nucl. Sci. Eng. 160 (2008) 385–400.
[4] S.G. Hong, Two subcell balance methods for solving the multigroup discrete ordinates transport equation with tetrahedral meshes, Nucl. Sci. Eng. 173 (2013) 101–117.
[5] S.G. Hong, Y.O. Lee, Subcell balance methods with linear discontinuous expansion for S_N transport calculation on tetrahedral meshes, Trans. Am. Nucl. Soc. 103 (2010) 354.
[6] S.G. Hong, J.W. Kim, Y.O. Lee, Development of MUST (Multi-Group Unstructured Geometry SN Transport) Code, in: Transaction of Korean Nuclear Society Autumn Meeting, Gyeong-ju, Korea, October 29-30, 2009.
[7] M.L. Adams, E.W. Larsen, Fast iterative methods for discrete ordinates particle transport calculations, Prog. Nucl. Energy 40 (2002) 3–159.
[8] R.E. Alcouffe, Diffusion synthetic acceleration methods for diamond difference discrete ordinates equations, Nucl. Sci. Eng. 64 (1977) 344–355.
[9] M.L. Adams, W.R. Martin, Diffusion synthetic acceleration of discontinuous finite element transport iterations, Nucl. Sci. Eng. 111 (1992) 145–167.
[10] K. Hussein, Effectiveness of a consistently formulated diffusion synthetic acceleration approach, Nucl. Sci. Eng. 98 (1988) 226–243.
[11] J.S. Warsa, T.A. Wareing, J.E. Morel, Fully consistent diffusion synthetic acceleration of linear discontinuous S_N transport discretizations on unstructured tetrahedral meshes, Nucl. Sci. Eng. 141 (2002) 236–251.
[12] H. Muhammad, S.G. Hong, Diffusion Synthetic Acceleration (DSA) for the Linear Discontinuous Expansion Method with Subcell Balance (LDEM-SCB), Transaction of Korean Nuclear Society, Jeju, Korea, May 16-18, 2017.
[13] T.A. Wareing, E.W. Larsen, M.L. Adams, Diffusion accelerated discontinuous finite element schemes for the S_N equations in slab and X-Y geometries, in: Proc. International Topical Meetings on Advances in Mathematics, Computations, Reactor Physics, Pittsburgh, Pennsylvania, vol. 3, 28 April – 2 May 1991, 1-1.
[14] Y. Wang, J.C. Ragusa, Diffusion synthetic acceleration for high order discontinuous finite element S_N transport schemes and application to locally refined unstructured meshes, Nucl. Sci. Eng. 166 (2010) 145–166.
[15] A.R. Owens, J. Kophazi, M.D. Eaton, Optimal trace inequality constants for interior penalty discontinuous Galerkin discretisations of elliptic operators using arbitrary elements with non-constant Jacobians, J. Comput. Phys. 350 (2017) 847–870.
[16] J.S. Warsa, T.A. Wareing, J.E. Morel, Krylov iterative methods and the degraded effectiveness of diffusion synthetic acceleration for multidimensional S_N calculations in problems with material discontinuities, Nucl. Sci. Eng. 147 (2004) 218–248.
[17] Y. Saad, Iterative Methods for Sparse Linear Systems, second ed., Society for industrial and applied mathematics, Philadelphia, Pennsylvania, 2003.
[18] H. Muhammad, S.G. Hong, Effective Use of the Linear Fine Mesh Rebalance for the DSA of S_N Transport Equation with Tetrahedral Meshes, vol. 118, Transaction of American Nuclear Society, Philadelphia, Pennsylvania, 2018.
[19] A. Yamamoto, Generalized coarse mesh rebalance method for acceleration of neutron transport calculations, Nucl. Sci. Eng. 151 (2005) 274–282.
[20] A. Yamamoto, Y. Kitamura, T. Ushio, N. Sugimura, Convergence improvement of coarse mesh rebalance method for neutron transport calculations, J. Nucl. Sci. Technol. 41 (2004) 781–789.
[21] S.G. Hong, K.S. Kim, J.S. Song, Fourier convergence analysis of the rebalance methods for discrete ordinates transport equations in eigenvalue problems, Nucl. Sci. Eng. 164 (2010) 33–52.
[22] S.G. Hong, N.Z. Cho, A rebalance approach to nonlinear iteration for solving the neutron transport equations, Ann. Nucl. Energy 24 (1997) 144–160.
[23] H. Muhammad, S.G. Hong, A three-dimensional fourier analysis of fine mesh rebalance acceleration of linear discontinuous sub-cell balance method for diffusion equation on tetrahedral meshes, Ann. Nucl. Energy 133 (2019) 145–153.